Disparate Midlatitude Responses to the Eastern Pacific El Niño

AUTHOR(S):

Shiozaki, Masahiro; Enomoto, Takeshi; Takaya, Koutarou

Disparate Midlatitude Responses to the Eastern Pacific El Niño

MASAHIRO SHIOZAKI,[a,e] TAKESHI ENOMOTO,[b,c] AND KOUTAROU TAKAYA[d]

[a] *Graduate School of Science, Kyoto University, Kyoto, Japan*
[b] *Disaster Prevention Research Institute, Kyoto University, Kyoto, Japan*
[c] *Application Laboratory, Japan Agency for Marine-Earth Science and Technology, Yokosuka, Japan*
[d] *Department of Astrophysics and Atmospheric Sciences, Kyoto Sangyo University, Kyoto, Japan*

(Manuscript received 8 April 2020, in final form 11 September 2020)

ABSTRACT: To investigate the disparate influences of the eastern Pacific (EP) El Niño on the winter climate in the Far East, we conducted composite analyses using long-term reanalysis datasets. Our analysis shows that the western Pacific (WP) pattern dominates in the warm winter (typical) composite and the Pacific–North American (PNA) pattern dominates in the non-warm winter (atypical) composite. In the warm winter case, the amplitudes of the negative sea surface temperature (SST) anomalies in the western Pacific Ocean are large whereas in the non-warm winter case, these amplitudes are small. In addition, the Indian Ocean basin warming occurs following the Indian Ocean dipole mode, as seen in the warm winter composite. We investigated the dynamical mechanisms responsible for the disparate midlatitude responses to the EP El Niño by focusing on Rossby wave sources and propagation. These SST anomalies modulate the Walker and Hadley circulations and the convective activity in the western Pacific Ocean. Upper-tropospheric divergences at the midlatitudes due to the anomalous Hadley circulation result in different teleconnection patterns. In the warm winter composite, the anticyclonic anomaly in the southern part of the WP pattern is created by the upstream negative Rossby wave source, while the other cyclonic anomaly is reinforced by the northward Rossby wave propagation. The cyclonic second and fourth centers of action of the PNA pattern are created by the positive Rossby wave sources. Furthermore, the equatorial SST gradient near the date line is found be a good precursor of the winter climate in the Far East.

KEYWORDS: Atmosphere-ocean interaction; El Nino; Pacific-North American pattern/oscillation; Rossby waves; Teleconnections; Winter/cool season

1. Introduction

In recent years, El Niño–Southern Oscillation (ENSO) diversity has received considerable attention, which in turn is categorized by the various sea surface temperature (SST) anomaly distributions or outstanding teleconnection patterns. Ashok et al. (2007) found a variation similar to El Niño in the second mode of the empirical orthogonal function (EOF) of SSTs in the Pacific Ocean since 1980, which they termed El Niño Modoki. In more recent studies, El Niño is usually called the eastern Pacific (EP) El Niño, whereas El Niño Modoki is often called the central Pacific (CP) El Niño (Kao and Yu 2009). The EP and CP El Niño differ in terms of their convection anomalies over the Pacific Ocean due to their different distributions of the SST anomalies that lead to the unique midlatitude responses. During an EP (a CP) El Niño, East Asia tends to be warmer (colder) than normal from winter to spring (Halpert and Ropelewski 1992; Yuan and Yang 2012).

Wang et al. (2000) proposed a mechanism of how the EP El Niño affects East Asian winter climate. According to their proposed mechanism, the southerly wind anomalies on the western side of the anticyclonic circulation, which are excited by negative SST anomalies in the Philippine Sea, contribute to the warm winters. However, some EP El Niño cases do not bring warm winters to East Asia. In the development of the anticyclonic circulation anomaly in the Philippine Sea, the Walker circulation anomaly associated with the Indian Ocean basin warming plays an important role (Watanabe and Jin 2002). The Indian Ocean basin warming seems to depend on the season in which a divergent easterly wind (DEW) in the Indian Ocean spreads during EP El Niño (Ohba and Ueda 2005). In their experiments, if the DEW is dominant from summer, the Indian Ocean dipole mode (IOD; Saji et al. 1999) occurs in the following fall. However, if the DEW is dominant from fall, the basin warming occurs in the following winter, without the IOD.

Kodera (1998) discovered that two types of the EP El Niño exist, one dominated by a Pacific–North American (PNA) pattern and the other by a western Pacific (WP) pattern, and that these two patterns do not tend to occur simultaneously. He also found that the SST anomaly in the equatorial central Pacific Ocean of the WP type was approximately 0.6 K warmer than that of the PNA type, but he did not discuss the excitation mechanisms for the different teleconnection patterns due to the SST anomaly. Because the PNA pattern during EP El Niño has been interpreted as the Rossby wave propagation from Hawaii to the western Atlantic Ocean as a response to the tropical SST anomalies (Horel and Wallace 1981; Hoskins and

Denotes content that is immediately available upon publication as open access.

[e] Current affiliation: Research Institute for Applied Mechanics, Kyushu University, Fukuoka, Japan.

Corresponding author: Masahiro Shiozaki, shiozaki.masahiro.27e@kyoto-u.jp

DOI: 10.1175/JCLI-D-20-0246.1

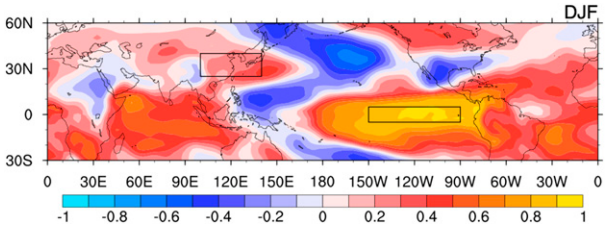

FIG. 1. The correlation coefficient of the 850-hPa temperature anomalies with respect to the Niño-3 index. Winters (DJF) in 1948–2018 are used. The two boxes are the "Far East"' (left box) and the Niño-3 region (right box).

Karoly 1981), one would expect a PNA pattern with warmer SST anomaly in the equatorial central Pacific Ocean. Therefore, the relationship between the two teleconnection patterns and the EP El Niño needs a consistent dynamical explanation. On the other hand, the relationship between the Pacific decadal oscillation (PDO) and ENSO has been investigated. Wang et al. (2008) pointed out that winters in East Asia during El Niño tend to be cold in the low phase of the PDO but did not argue about height anomalies in the middle and upper troposphere. However, their results indicate dominant teleconnection patterns are different between the high and low phases of the PDO.

The southern center of the WP pattern may be excited by an atmospheric diabatic heating anomaly in the Philippine Sea. Ueda et al. (2015) showed that an atmospheric diabatic heating anomaly in the Philippine Sea can excite a cyclone in the lower troposphere over China as a baroclinic Rossby wave response (Matsuno 1966; Gill 1980). In addition, the eastward propagation of the stationary Rossby wave along the westerlies can create an anticyclone in the upper troposphere around Japan, which can be interpreted as the southern center of action of the WP pattern. To test this hypothesis, investigations of Rossby wave sources and propagation are required. Therefore, in this present work, we attempt to answer an open research question on the mechanisms how the distributions of tropical SST anomalies during EP El Niño yield the disparate teleconnection patterns and bring the different winter climate in the Far East.

Of course, the East Asian winter monsoon (EAWM) strongly influences the winter climate in the Far East. The activity of the EAWM is modulated by the circulation patterns in the upper troposphere: a WP-like pattern with the meridional dipole in the northwestern Pacific Ocean and a Eurasian (EU)-like pattern with a wave train over the Eurasian continent (Takaya and Nakamura 2013). The fact that the WP-like pattern modulates the EAWM implies some influence from the tropics. Hence, we will also examine the significance of the EU-like pattern during ENSO.

We present the datasets used for this study and our analysis methods in section 2, while section 3 shows the results of our composite analyses. Therein, the temperature and height anomalies are used to identify the midlatitude response characteristics in each composite in section 3a. Then the SST and diabatic heating anomalies are examined in sections 3b and 3c, respectively. In section 3d, we examine the relationship between the tropical heating and the teleconnection patterns using the Rossby wave source and wave activity analyses. The predictability of the anomalous weather in the Far East is discussed in section 3e. Finally, we summarize this study in section 4. Hereafter, EP El Niño is denoted simply as El Niño.

2. Method and datasets

a. *Datasets and the definition of ENSO and teleconnection patterns*

Monthly Extended Reconstructed Sea Surface Temperature (ERSST) v5 data (Huang et al. 2017) on a 2.0° × 2.0° horizontal grid for the years 1918 to 2018 obtained from the National Oceanic and Atmospheric Administration (NOAA) have been used to identify ENSO events and to analyze the SST distributions. For the extracted ENSO events, the National Centers for Environmental Prediction (NCEP)–National Center for Atmospheric Research (NCAR) monthly mean Reanalysis 1 (Kalnay et al. 1996) on a 2.5° × 2.5° horizontal grid for the years 1948 to 2018 have been used to analyze temperature, height, wind, sea level pressure (SLP), Rossby wave source anomalies, and wave activity fluxes. Japanese 55-year Reanalysis (JRA-55; Kobayashi et al. 2015) data on a 1.25° × 1.25° horizontal grid for the years 1958 to 2018 obtained from the Japan Meteorological Agency (JMA) have been used to analyze diabatic heating. There is almost no difference between atmospheric responses using JRA-55 and using NCEP reanalysis data. NCEP reanalysis data are mainly used in this study because the period is longer than JRA-55. However, JRA-55 is used for the analysis of diabatic heating because NCEP reanalysis data do not have diabatic heating data. The diabatic heating in this study is a summation of the large-scale condensation, convective, vertical diffusion, solar radiative, and longwave radiative heating rates and vertical integration of the summation from the surface to 200 hPa.

We have adopted the definition made by the JMA to identify ENSO events during winter months from 1948 to 2018 as follows. An El Niño (La Niña) event is a period when the ENSO indices are consecutively above +0.5 (−0.5) K for 6 months or longer. A monthly ENSO index is calculated as a 5-month running mean of SST anomalies from a reference value in the Niño-3 region (5°S–5°N, 90°–150°W). The reference value for each month is calculated as a 30-yr average until the previous year. The reference values are renewed every year for each month; hence, the global warming trend is eliminated from the index.

To compare with the intensity of teleconnection patterns, teleconnection pattern indices are calculated based on the definition of teleconnection patterns (Wallace and Gutzler 1981).

b. *Statistical analysis*

We have examined the temperatures, heights, SSTs, circulation, and Rossby wave source anomalies and wave activity fluxes during winter [December–February (DJF)], that is, at a time when almost all the ENSO indices demonstrated peak values. Anomalies have been obtained as the difference from the global warming trend during winter that was calculated by linear least squares method from 1948. The identified El Niño events have been classified into warm or a non-warm winter

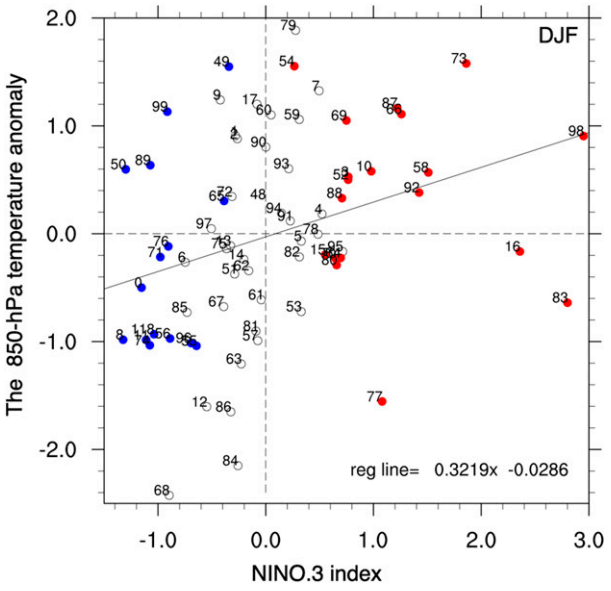

FIG. 2. Relationship between the Niño-3 indices (x axis) and the 850-hPa temperature anomalies in the Far East (y axis). The red, white, and blue dots denote El Niño, non-ENSO, and La Niña cases, respectively. The number to the upper left of each dot shows the year based on January. The regression line is estimated from all points.

cases using the 850-hPa temperature anomaly in the Far East (25°–40°N, 100°–140°E). This region has been chosen based on the correlation coefficients between the Niño-3 index and the winter 850-hPa temperature anomaly (Fig. 1) and designated as the Far East, as it can capture the activity of the EAWM (Takaya and Nakamura 2013).

Composite analyses have been conducted on three categories: 1) the average of all El Niño cases (hereafter ALL), as well as 2) warm winter and 3) non-warm winter composites. To confirm statistical significance, the Student's t test has been used for all three categories. Additionally, Welch's t test has been used to calculate the statistical significance of the differences between the warm and non-warm cases because the variances of the warm and the non-warm winter composites were unknowns. Welch's t statistic for each grid point was calculated as

$$t(\overline{x_w}, \overline{x_n}, s_w^2, s_n^2) = \frac{\overline{x_w} - \overline{x_n}}{\sqrt{\frac{s_w^2}{N_w} + \frac{s_n^2}{N_n}}}$$

where the variances s_w have the form

$$s_w^2 = \frac{\sum_i (x_{wi} - \overline{x_w})^2}{N_w - 1}.$$

Similarly, s_n is the same form but for the subscript n. Here, subscripts w and n represent warm and non-warm winter cases, respectively; x is the sample, the overline signifies an average, s^2 is the variance, and N is the number of samples. The statistic $t(\overline{x_w}, \overline{x_n}, s_w^2, s_n^2)$ follows the t distribution with degrees of freedom m derived for each grid points as follows and approximated to the nearest integer value:

$$m = \frac{\left(\frac{s_w^2}{N_w} + \frac{s_n^2}{N_n}\right)^2}{\frac{s_w^4}{N_w^2(N_w - 1)} + \frac{s_n^4}{N_n^2(N_n - 1)}}.$$

c. *Analysis of the Rossby wave sources and the wave activity fluxes*

Teleconnection patterns in height anomalies (Wallace and Gutzler 1981) in the warm and the non-warm winter composites were diagnosed using the Rossby wave sources (Sardeshmukh and Hoskins 1988) and the wave activity fluxes (Takaya and Nakamura 2001). To clarify the relationship between convective activity in the tropics associated with tropical SST anomalies and height anomalies at the midlatitudes, we calculated the Rossby wave source S using the following equation derived from the barotropic vorticity equation under the assumption of negligible friction:

$$\left(\frac{\partial}{\partial t} + \mathbf{v}_\psi \cdot \nabla\right)\zeta = S,$$

where $\mathbf{v}_\psi$ is the rotational winds, ζ is the vorticity, and $S = -\mathbf{v}_\chi \cdot \nabla\zeta - \zeta\nabla \cdot \mathbf{v}_\chi$, where $\mathbf{v}_\chi$ is the divergent winds. By separating $\mathbf{v}_\chi$ and ζ into the climatology (denoted by an overline) and perturbation (denoted by a prime) components, the Rossby wave source anomaly is represented by

$$\begin{aligned} S' &= -\nabla \cdot (\mathbf{v}_\chi'\overline{\zeta}) - \nabla \cdot (\overline{\mathbf{v}_\chi}\zeta') \\ &= -\overline{\zeta}D' - \mathbf{v}_\chi' \cdot \nabla\overline{\zeta} - \zeta'\overline{D} - \overline{\mathbf{v}_\chi} \cdot \nabla\zeta', \end{aligned}$$

where $D = \nabla \cdot \mathbf{v}_\chi$.

The propagation of Rossby waves is represented by the horizontal components of the wave activity flux for zonally non-uniform basic fields under the quasigeostrophic balance:

$$W = \frac{p\cos\phi}{2\sqrt{\overline{u}^2 + \overline{v}^2}} \begin{pmatrix} \frac{\overline{u}}{a^2\cos^2\phi}\left[\left(\frac{\partial\psi'}{\partial\lambda}\right)^2 - \psi'\frac{\partial^2\psi'}{\partial\lambda^2}\right] + \frac{\overline{v}}{a^2\cos\phi}\left[\frac{\partial\psi'}{\partial\lambda}\frac{\partial\psi'}{\partial\phi} - \psi'\frac{\partial^2\psi'}{\partial\lambda\partial\phi}\right] \\ \frac{\overline{u}}{a^2\cos\phi}\left[\frac{\partial\psi'}{\partial\lambda}\frac{\partial\psi'}{\partial\phi} - \psi'\frac{\partial^2\psi'}{\partial\lambda\partial\phi}\right] + \frac{\overline{v}}{a^2}\left[\left(\frac{\partial\psi'}{\partial\phi}\right)^2 - \psi'\frac{\partial^2\psi'}{\partial\phi^2}\right] \end{pmatrix},$$

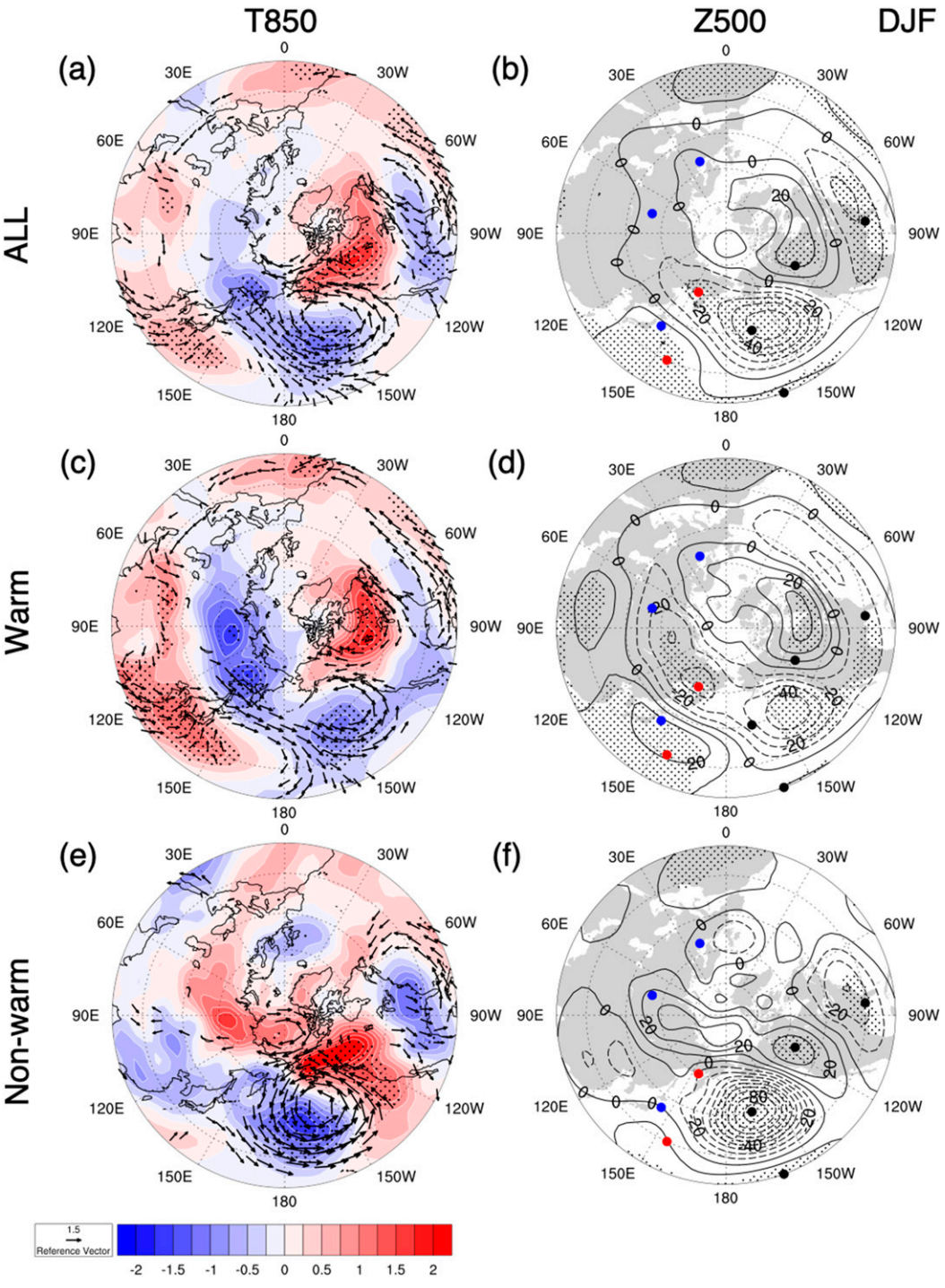

FIG. 3. (a),(c),(e) The temperature anomalies (color shades; K) and the wind anomalies (arrows; m s^{-1}) in the 850-hPa composites and (b),(d),(f) height anomalies (contours; m) in the 500-hPa composites for (a),(b) ALL, (c),(d) warm winter, and (e),(f) non-warm winter cases. The contour interval is 10 m. The arrows and hatches show anomalies with a statistical significance of 90%. The dots in black, red, and blue indicate the centers of action of the PNA, WP, and EU patterns, respectively.

where p is the normalized pressure (pressure/1000 hPa), u and v are the zonal and meridional winds averaged for 30 years (1981–2010), a is the radius of Earth, and ϕ and λ are the latitude and the longitude, respectively. Furthermore, the quasi-geostrophic streamfunction anomaly ϕ' is defined as $\psi' = \Phi'/f$ using the geopotential anomaly and the Coriolis parameter f.

3. Results

Figure 2 shows the relationship between the Niño-3 index and the 850-hPa temperature anomalies in the Far East. The t value of regression is 2.750, the standard error of the regression coefficient is 0.117, and the number of cases is 71 (DJF in 1948–2017/18), which yields 69 degrees of freedom (degree of freedom is number of cases minus 2). To test at the two-tailed 95% level, we note that $t(69)$ is ± 1.995. Clearly, the calculated t statistic greatly exceeds 1.995. So, this regression coefficient shows statistical significance of 95%.

There are 19 cases of El Niño that have occurred since 1948, among which 12 cases (63%) in the first quadrant are used in the warm winter composites and 7 cases (37%) in the fourth quadrant are used in the non-warm winter composite. The warm winter composite includes the 1951/52, 1953/54, 1957/58, 1965/66, 1968/69, 1972/73, 1986/87, 1987/88, 1991/92, 1997/98, 2002/03, and 2009/10 cases, and the non-warm winter composite includes the 1963/64, 1969/70, 1976/77, 1979/80, 1982/83, 2014/15, and 2015/16 cases. Figure 2 suggests that strong El Niño cases (Hameed et al. 2018) do not necessarily exhibit corresponding large temperature anomalies in the Far East (Shiozaki and Enomoto 2020).

a. *Temperature anomalies and teleconnection patterns*

Composite analyses of temperature and height anomalies were conducted to investigate influences on winter climate and atmospheric circulation. Figure 3 shows the 850-hPa temperature and 500-hPa height anomalies and Table 1 shows the teleconnection pattern indices of the PNA, WP, and EU patterns. In ALL (Fig. 3a), the southerly wind anomalies are dominant in the Far East to bring a statistically significant warm winter. Additionally, the PNA pattern is dominant with a PNA index of 0.66 (Fig. 3b). In the northwestern Pacific Ocean, a positive height anomaly is located over Japan and a negative anomaly extending from the Aleutians to Okhotsk is located to the north of the positive anomaly with a WP index of −0.66.

In the warm winter composite (Fig. 3c), the warm region in the Far East spreads wider than that in ALL. In the height anomalies (Fig. 3d), while the WP pattern is dominant with a WP index of −0.85, the PNA pattern is less clear, as reflected by its PNA index of 0.42. A pair of positive negative height anomalies near Japan corresponds to the WP type during El Niño in Kodera (1998) and is similar to warm winter with the WP pattern in Takaya and Nakamura (2013).

In the non-warm winter composite (Fig. 3e), the temperature anomalies in the Far East of approximately −0.5 K are not statistically significant. This cold anomaly is accompanied by a negative height anomaly (Fig. 3f) over northeastern China (approximately 45°N, 115°E), which might be regarded as an EU-like pattern (Takaya and Nakamura 2013). However, the EU-like pattern is not accompanied by Rossby wave flux (see section 3d) and cannot be regarded as Rossby wave propagation. In addition, a dominant PNA pattern with a PNA index of 1.06 corresponds to the PNA type during El Niño in Kodera (1998).

According to Fig. 3 and Table 1, the outstanding teleconnection patterns are the PNA and WP-like dipole patterns in ALL, the WP and less clear PNA patterns in the warm winter composite, and a clear PNA pattern in the non-warm winter composite. The EU pattern is an essential teleconnection pattern that influences on winter climate in East Asia, but the EU index is small and the PNA and/or WP indices are large for all classification. This suggests the importance of the external forcing associated with El Niño for exciting the PNA or the WP pattern.

Next, before we examine the mechanisms for the different teleconnection patterns, we will examine the characteristic SST distributions and diabatic heating in the following two sections.

b. *Anomalous SST and lower-tropospheric winds in the tropics*

In this section, we show SST averages for each classification to confirm the mechanism bringing warm winter to East Asia (Wang et al. 2000) and clarify the deviations between the warm and non-warm winter cases.

Figure 4 shows the composites of tropical SST and circulation anomalies. In ALL (Fig. 4a), negative SST anomalies exhibit a horseshoe-shaped distribution in the Pacific Ocean. Southerly wind anomalies toward the Far East due to a positive SLP anomaly are dominant in the Philippine Sea (centered at approximately 15°N, 130°E), which contribute to the warm winter in the Far East. Additionally, statistically significant positive SST anomalies are distributed from the Maritime Continent to the Indian Ocean. These SST and SLP anomaly distributions are consistent with those found by Wang et al. (2000). Moreover, the Indian Ocean basin warming corresponds to suppressed convection in the western Pacific Ocean through a Walker circulation anomaly. This is consistent with the experimental results found by Watanabe and Jin (2002).

In the warm winter composite (Fig. 4b), the distributions of the SST and circulation anomalies are similar to those of ALL, but with larger amplitudes. In the Indian Ocean, the SST anomalies indicate basin warming and a Ningaloo Niña–like along the western coast of Australia (Feng et al. 2013; Kataoka et al. 2014). This SST distribution is similar to that during weak EAWM, suggesting the influence of SST in the Indian Ocean on the EAWM (Wang and Chen 2014). However, the amplitude of SST anomaly in the western Pacific Ocean in this study is larger than in the previous study. We will show the importance of the SST anomaly in the western Pacific Ocean to the EAWM in a later section.

Conversely, in the non-warm winter composite (Fig. 4c), the center of the positive SST anomaly distribution in the equatorial eastern Pacific Ocean is slightly shifted to the east compared with that in the warm winter composite. Moreover, the negative SST anomalies demonstrate smaller amplitudes in the western Pacific Ocean (within approximately 0°–15°N, 130°–160°E). As a result, the amplitude of the positive SLP

TABLE 1. Teleconnection pattern indices of each classification.

	ALL	Warm winter	Non-warm winter
PNA	0.66	0.42	1.06
WP	−0.66	−0.85	−0.34
EU	−0.17	−0.43	0.29

anomaly in the Philippine Sea is small, and no statistically significant southerly wind anomalies toward the Far East occur. In the Indian Ocean, the negative SST anomalies off the western coast of Australia are absent because the easterly wind anomalies from the Maritime Continent exhibits a limited zonal extent. This is consistent with a reduced convective suppression in the western Pacific Ocean. In the Atlantic Ocean, the easterly wind anomalies along the equator are stronger than those in the warm winter composite. The amplitude of the SST anomalies in the Caribbean Sea are also larger, but this result is not statistically significant.

The features discussed above are clearly shown in the differences of the SST and the horizontal circulation anomalies in the tropics between the warm and the non-warm winter composites (Fig. 5). The SST difference in the central Pacific Ocean (approximately 10°N–10°S, 180°–140°W) is approximately 0.5 K (statistically significant), consistent with the difference of the SST between the WP and the PNA types identified by Kodera (1998). Additionally, a statistically significant difference of approximately −0.3 K exists in the western Pacific Ocean (approximately 15°N–10°S, 130°–170°E), which is not statistically significant in the study by Kodera (1998), probably due to a limited number of events.

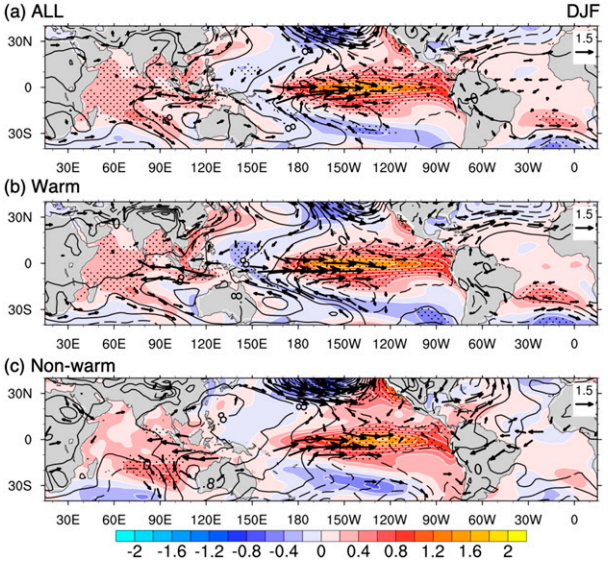

FIG. 4. SST (color shades; K), SLP (contours; hPa), and wind (arrows; m s^{-1}) anomalies at the 850-hPa surface in the DJF composite for (a) ALL, (b) warm winters, and (c) non-warm winters. The arrows and hatches show anomalies with a statistical significance of 90%.

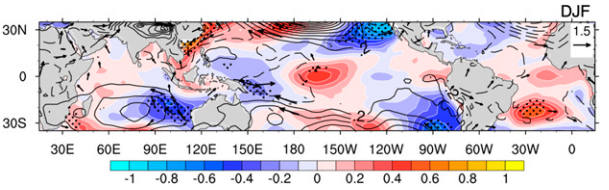

FIG. 5. Differences (i.e., the warm composite minus the non-warm winter composite) of the SST (color shades; K), SLP (contours; hPa), and wind (arrows; m s^{-1}) anomalies at the 850-hPa surface in DJF. Zero contours are omitted. Scaling for the arrows is given near the upper-right corner. The arrows and hatches show anomalies with a statistical significance of 90%.

c. *Heating anomalies and associated modulation of the Walker circulation*

The SST anomalies in the tropics and associated changes in convective activity result in atmospheric heating anomalies. In this section, we investigate atmospheric heating anomalies in the tropics, which affect the atmospheric responses at the midlatitudes. Note that the warm winter cases do not include 1951/52 and 1953/54 because of the limited coverage of the JRA-55 dataset during these years.

In all three cases (Figs. 6a–c), the distributions of the tropical heating anomalies are similar to those of the tropical SST anomalies (Fig. 4) but different in that a negative heating anomaly is located at approximately 10°N, corresponding to a shift of the intertropical convergence zone (ITCZ). The negative heating anomaly in the Philippine Sea (approximately 10°N, 130°E) corresponds to the positive SLP anomaly and the

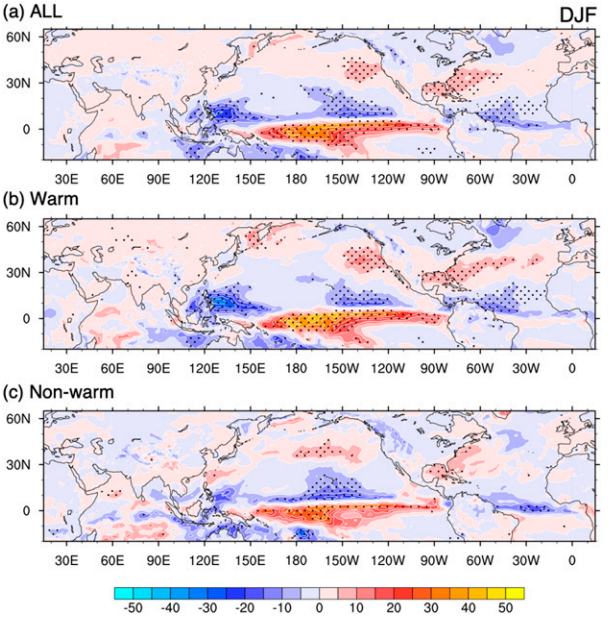

FIG. 6. As in Fig. 4, but for diabatic heating anomalies (color shades; K day^{-1}) integrated from the surface to 200-hPa surface.

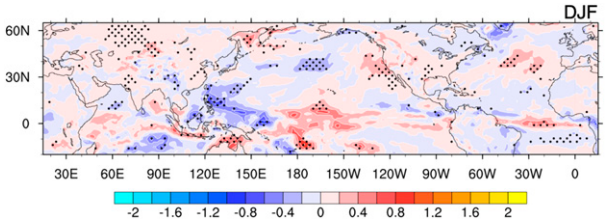

FIG. 7. As in Fig. 5, but for the diabatic heating anomalies (color shades; K day^{-1}) integrated from the surface to 200-hPa surface.

weakened Walker circulation. The largest amplitude of the heating anomaly is due to convection and the others are very small (figure omitted). The heating anomalies due to convection along the Far East are small in both cases.

In the warm winter composite (Fig. 6b), the amplitude of the negative heating anomaly in the Philippine Sea is larger because the Walker circulation is more modulated, strongly due to the larger SST anomaly zonal gradient in the western Pacific Ocean (Fig. 4b). This is consistent with the dominance of a negative SLP anomaly in China, a positive SLP anomaly in regions east of Japan, and the southern part of the WP pattern (Ueda et al. 2015).

At the midlatitudes, the locations of positive heating anomalies are consistent with those of the 500-hPa height anomalies seen in Fig. 3d. The positive heating anomaly in the Sea of Okhotsk is probably created by a cold flow from the Eurasian continent and exhibits a limited vertical extent below 850 hPa (not shown), consistent with a negative temperature anomaly at the 850-hPa surface (Fig. 3c) that may contribute to an increased sea ice extent (not shown).

In the non-warm winter composite (Fig. 6c), the amplitudes of the positive heating anomalies along the equator and the negative heating anomalies in the Philippine Sea are smaller than those in the warm winter composite. Thus, convection in the western Pacific Ocean in the non-warm winter composite is suppressed less extensively than that in the warm winter composite. However, the statistically significant negative heating anomaly along the 10°N is extended more to the west than that in the warm winter composite.

At the midlatitudes, statistically significant positive heating anomalies with statistical significance are located in the north-central Pacific Ocean and in the vicinity of the eastern coast of the United States but not in the Sea of Okhotsk (Fig. 6c). This distribution is consistent with the absence of a statistically significant cold flow from the Eurasian continent (Fig. 3e).

Figure 7 shows the difference in the heating anomalies to clarify the dissimilarity between the warm and the non-warm winter composites. The differences in the heating anomalies bear close resemblances to those of the SST anomalies in the Pacific Ocean (Fig. 5). While two zonal dipoles of the differences exist in the equatorial western-central and the north-northeastern Pacific Ocean, very few differences are found in the SST anomalies on the Indian Ocean. Especially, the negative heating anomaly in the western Pacific Ocean is remarkable for the difference between warm and non-warm winter cases. Ueda et al. (2015) pointed out the relationship whereby heating anomaly in the Philippine Sea affects the

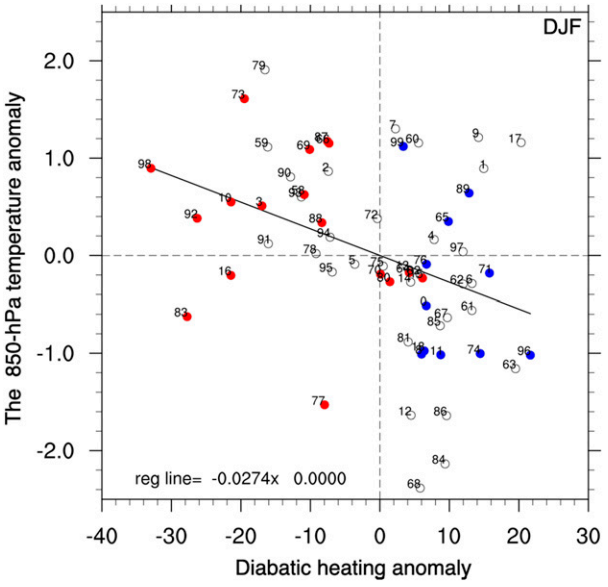

FIG. 8. As in Fig. 2, but for the diabatic heating anomalies in the Niño-3 region (0°–15°N, 130°–150°E; x axis) and the 850-hPa temperature anomalies in the Far East (y axis).

temperature anomaly around Japan. Figure 8 shows the relationship between heating anomalies in the Philippine Sea and the 850-hPa temperature anomalies in the Far East. The t value of regression is −4.348, the standard error of the regression coefficient is 0.073, and the number of cases is 71 (DJF in 1948–2017/18), which yields 69 degrees of freedom (degree of freedom is the number of cases minus 2). To test at the two-tailed 95% level, we note that $t(69)$ is ±1.995. Clearly, the calculated t statistic greatly exceeds 1.995. So, this regression coefficient shows a statistical significance of 95%. The scatterplot shows that their claim is also valid for El Niño cases. The notable exceptions in the 1982/83 and the 2015/16 cases can be explained by vorticity balance in the midlatitude (Shiozaki and Enomoto 2020). In the next section, we will investigate Rossby wave sources and propagations in the upper troposphere to test the hypothesis that the response in East Asia is due to the Rossby wave propagation (Ueda et al. 2015).

d. Rossby wave sources and propagation

In the previous two sections, we have seen that differences in SST anomalies cause differences in convective activity and the associated Walker and Hadley circulations. Indeed, divergences due to convective activity in turn generate Rossby wave sources. Figure 9 shows the 250-hPa Rossby wave source anomaly. Common features of the three classifications are as follows: 1) the centers of action of the PNA pattern are located between the positive and negative Rossby wave sources and consistent with the vorticity balance in the midlatitudes (Honda et al. 1999), and 2) a divergent area in the northern Pacific Ocean is superposed on the positive heating anomalies (Fig. 7).

In the warm winter composite (Fig. 9b), a negative wave source anomaly (approximately 35°N, 130°E) is located to the west of a positive height anomaly (approximately 35°N, 140°E).

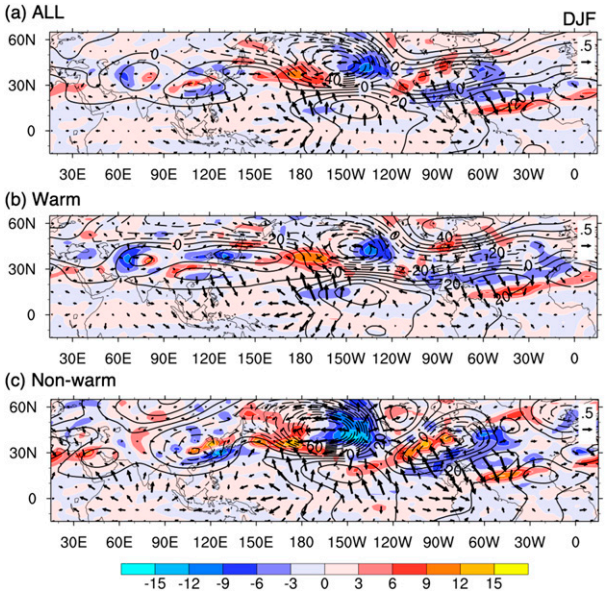

FIG. 9. As in Fig. 4, but for Rossby wave sources (color shades; s^{-2}), height (contours; m), and divergent wind (arrows; $m\,s^{-1}$) anomalies at the 250-hPa surface.

The negative source anomaly is due to the divergence anomaly associated with the local Hadley circulation in response to the suppressed convection in the equatorial western Pacific Ocean (approximately 135°E). The positive height anomaly is in balance with the upstream negative vorticity source. Thus, the convective suppression in the equatorial western Pacific Ocean contributes to exciting the southern part of the WP pattern.

In the non-warm winter composite (Fig. 9c), the large-amplitude divergent wind anomalies are located in the equatorial central and eastern Pacific Ocean (approximately 180°–90°W), corresponding to the distribution of the eastward shifted positive SST anomalies (Fig. 4c). These divergent wind anomalies excite the positive Rossby wave sources corresponding to the second and fourth centers of action of the PNA pattern. Therefore, the PNA pattern in the non-warm winter composite is clearer than that in the warm winter composite.

Conversely, the divergent wind anomalies at the midlatitudes associated with the slowed local Hadley circulation in the western Pacific Ocean are weaker than that in the warm winter composite. This weaker divergence is consistent with the weak suppressed convection in the western Pacific Ocean. Thus, the Rossby wave source corresponding to the southern part of the WP pattern is not excited.

Next, we will examine whether a train of anomalies is caused by Rossby wave propagation. Figure 10 shows the 250-hPa wave activity flux for a zonally nonuniform basic field (Takaya and Nakamura 2001). In ALL (Fig. 10a), the wave activity fluxes near 25°N, 160°W show northeastward and southeastward divergence, corresponding to a acceleration of the westerly jet. This region is on the south side of the second center of action of the PNA pattern. The fluxes from approximately 20°N, 120°W diverge to the fourth center of action of the PNA

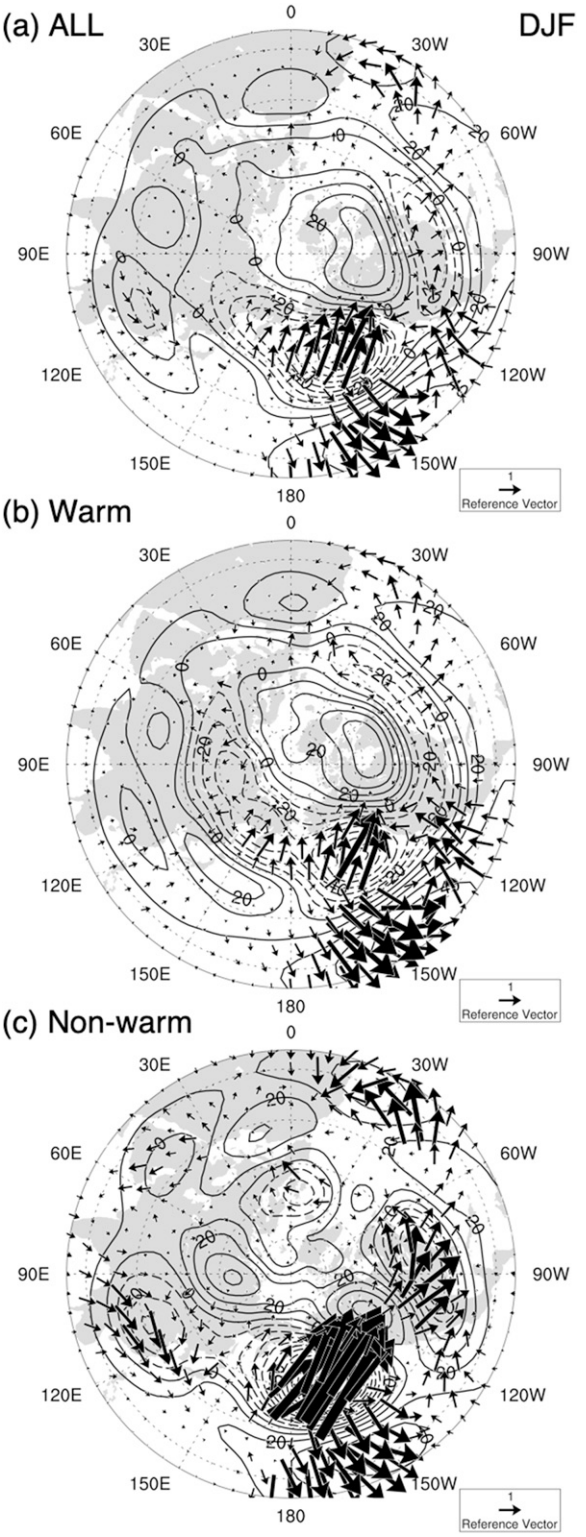

FIG. 10. As in Figs. 2b,d,f, but for height (contours; m) and wave activity flux (arrows; $m^2\,s^{-2}$) at the 250-hPa surface.

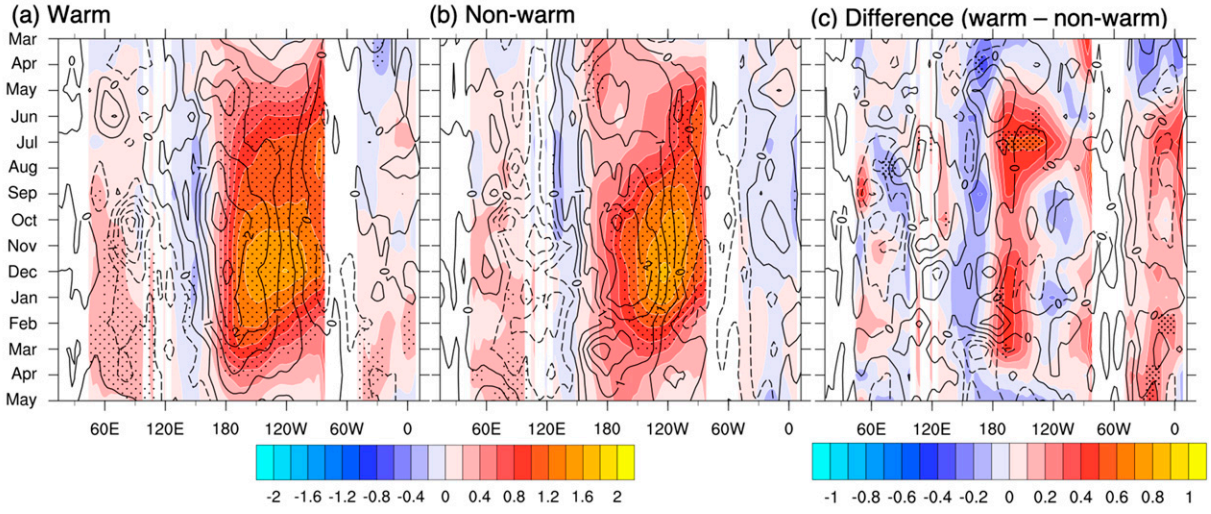

FIG. 11. Temporal evolution of the SST (color shades; K) and zonal wind (contours; m s^{-1}) anomalies at the 925-hPa surface averaged between 5°N and 5°S for (a) warm winter, (b) non-warm winter, and (c) the differences between them. The hatches show anomalies with statistical significance of 90%.

pattern and are merged with the fluxes from the third center. Moreover, in East Asia, the fluxes from the Bay of Bengal and the South China Sea propagate to the Far East. The starting points of these fluxes superpose on the positive Rossby wave sources (Fig. 9a).

In the warm winter composite (Fig. 10b), the wave activity flux distribution is similar to that of ALL. Northward wave activity fluxes exist around 60°N, 155°E, emanating from a positive Rossby wave source anomaly located around 50°N, 150°E. These fluxes act to reinforce the northern part of the WP pattern and are consistent with Rossby wave propagation related to the positive heating anomaly in the Sea of Okhotsk (Takaya and Nakamura 2001). Furthermore, the fluxes from approximately 20°N, 120°W do not rotate clockwise toward the East Coast of the United States. Additionally, the fluxes from the Bay of Bengal and the South China Sea are not found.

Conversely, in the non-warm winter composite (Fig. 10c), the fluxes propagating from approximately 20°N, 120°W and from the second center of action of the PNA to the fourth center are stronger than those in the warm winter composite, and these two branches merge near the east coast of the United States. These fluxes emanate from the Rossby wave sources located at approximately 40°N, 180° and 20°N, 130°W. Furthermore, the fluxes propagating from the Bay of Bengal and the South China Sea are significantly larger and converge at the south side of Japan. These fluxes may correspond to the negative heating anomaly located at approximately 5°–15°N, 85°–120°E (Figs. 6c and 7). Thus, the cyclone over northeastern China is generated not by the Rossby wave propagation associated with the EU pattern but instead from the Bay of Bengal.

e. A precursory signal of the winter climate in the Far East during El Niño

In this section, we investigate the development of tropical SST anomalies in the warm and the non-warm winter composites and examine whether the equatorial SST anomalies in the developing seasons may be regarded as a precursory signal of the winter climate in the Far East.

1) DIFFERENCES IN THE TEMPORAL EVOLUTIONS OF TROPICAL SST ANOMALIES

Figure 11 shows the temporal evolution of SST and wind anomalies in the lower troposphere along the equator (averaged between 5°N and 5°S). In the warm winter composite (Fig. 11a), positive SST anomalies in the eastern Pacific Ocean develop rapidly from late spring in the developing year to reach the date line. A peak appears in early winter near 120°W. The westerly wind anomalies maintain a maximum value to the east of the date line from the developing spring. In the western Pacific Ocean and the eastern Indian Ocean, the amplitudes of the easterly wind anomalies increase from the developing summer, and the IOD occurs in the developing fall. The easterly wind anomalies near 90°E are consistent with the onset of the IOD.

Conversely, in the non-warm winter composite (Fig. 11b), the positive SST anomalies with large amplitudes in the eastern Pacific Ocean extend only to the east of 120°W until the developing summer. However, the positive SST anomalies develop rapidly in the developing fall, and the peak exceeds that seen in the warm winter composite. The peak of the westerly wind anomalies is located to the east of the date line. In the Indian Ocean, positive SST anomalies extend around the whole equator, consistent with a weak Walker circulation anomaly because of the slower extension to the date line of the positive SST anomalies in the eastern Pacific Ocean and the weak easterly wind anomaly at approximately 120°E (Ohba and Ueda 2005).

Figure 11c shows the differences of the SST and zonal wind anomalies along the equator between the warm and non-warm winter composites. From the onset to the decay of the El Niño,

TABLE 2. Reclassification of El Niño cases using the standard deviation of the SST gradient in the equatorial central Pacific Ocean in JJA.

	$>1\sigma$	$\leq 1\sigma$
Warm	1953/54, 1957/58, 1965/66, 1972/73, 1987/88, 1997/98, 2002/03	1951/52, 1968/69, 1986/87, 1991/92, 2009/10
Non-warm	1982/83, 2015/16	1963/64, 1969/70, 1976/77, 1979/80, 2014/15

the SST anomaly gradients are large near the date line, and collocated with the difference peaks of the zonal wind anomalies. The divergence of zonal wind roughly corresponds to the convection in this area, where the wind is dominantly zonal. Therefore, the active areas of the convection are different between the warm and the non-warm winter composites: in the western and eastern Pacific Ocean for the warm and non-warm composites, respectively. In the Indian Ocean, the tendencies of the easterly wind anomalies and the IOD are clear in the warm winter composite from the late summer to early fall in the developing year.

2) Detection of a precursory signal based on tropical SST anomaly

The SST anomaly differences in the summer are the largest during the developing seasons (Fig. 11c). Consequently, we reclassified the El Niño cases in those possessing large and small SST anomaly gradients, using the differences in the area average of the SST anomalies between 5°N–5°S, 150°E–180° and 5°N–5°S, 180°–150°W. A threshold of one standard deviation, 1σ, is used. Table 2 shows the reclassified El Niño events. The majority of the warm winter composites are included in the $> 1\sigma$ cases but only the two super El Niño cases (the 1982/83 and 2015/16 cases) are included in the $> 1\sigma$ cases for the non-warm winter composite.

Figure 12 shows composites of 850-hPa temperature and 500-hPa height anomalies based on the reclassifications. In the $>1\sigma$ composites (Figs. 12a,b), it tends to be warm winter with southerly wind anomalies, and the WP pattern is dominant, as indicated by the teleconnection indices (Table 3): 0.72, −1.09, and −0.32 for PNA, WP, and EU patterns, respectively. These features remain for the $>1\sigma$ composite without the three super El Niño events (1982/83, 1997/98, and 2015/16; Figs. 12c,d). That is, the large SST anomalies due to the three super El Niño events do not greatly change the results. Therefore, these results are similar to those in the warm winter composites.

Conversely, in the $\leq 1\sigma$ composite (Figs. 12e,f), normal winter is seen, and the PNA pattern is dominant, as shown by the teleconnection indices (Table 3): the PNA index of 0.60, the WP index of −0.27, and the EU index of − 0.03. Therefore, these results are similar to those found in the non-warm winter composites.

Figure 13 shows the composites of the SST and the horizontal circulation anomalies based on the $>1\sigma$ cases. From June to August (JJA), the positive SST anomalies in the equatorial eastern Pacific Ocean expand to the date line and the large amplitude of the negative SST anomalies distributes in the western Pacific Ocean with statistical significance. The 850-hPa westerly wind anomalies are dominant from 120°E to 130°W. The statistically significant SST and the circulation anomalies are distributed only in the Pacific Ocean and not in the Indian Ocean during JJA.

During DJF, the positive SST anomalies in the eastern Pacific Ocean are amplified and the peak moves from 80°W to 140°W. The negative SST anomalies in the Philippine Sea are also amplified, and an anticyclonic circulation develops therein, but the SST anomalies in the western Pacific Ocean (approximately 0°–15°S, 140°–170°E) are attenuated. Furthermore, the easterly wind anomalies are dominant in the Maritime Continent and the eastern Indian Ocean, while the SST anomalies show a statistically significant basin warming, similar to those seen in the warm winter composite (Fig. 4b). The composite without the super El Niño cases (Fig. 14) also shares these features; however, the wind and the SST anomalies are not statistically significant because of the small number of cases considered. These features are similar to those seen in the warm winter composite (Fig. 4b).

In sharp contrast, the SST anomalies in the $\leq 1\sigma$ composite (Fig. 15) spread widely along the equatorial Pacific Ocean during JJA, consistent with a significantly smaller SST gradient in the central Pacific Ocean. This large positive anomaly is confined to the east of approximately 130°W, consistent with the wind anomalies, but it is not statistically significant.

During DJF, the positive SST anomalies in the eastern Pacific Ocean is amplified and its peak migrates westward from 90° to 150°W. The SST anomalies in the western Pacific and the Indian Oceans are not amplified. These SST distribution and amplitude are consistent with absence of easterly wind anomalies in the eastern Indian Ocean. This indicates that the suppression of convection in the western Pacific Ocean is weaker than that in the $>1\sigma$ composite. These features are, therefore, similar to those seen in the non-warm winter composite.

4. Summary and discussion

In this study, the relationship between the winter climate in the Far East and EP El Niño cases since 1948 was investigated using long-term atmospheric and SST reanalysis datasets. To clarify the dynamical processes of the influence of El Niño on the winter climate in the Far East, the extracted El Niño cases are classified into the warm and the non-warm winter cases based on the 850-hPa temperature anomalies in the Far East.

The warm winter composites were characterized by the dominant WP pattern (Fig. 3d), the negative SST anomalies in the western Pacific Ocean, and the basin warming in the Indian Ocean (Fig. 4b). The distribution of the negative SST and the

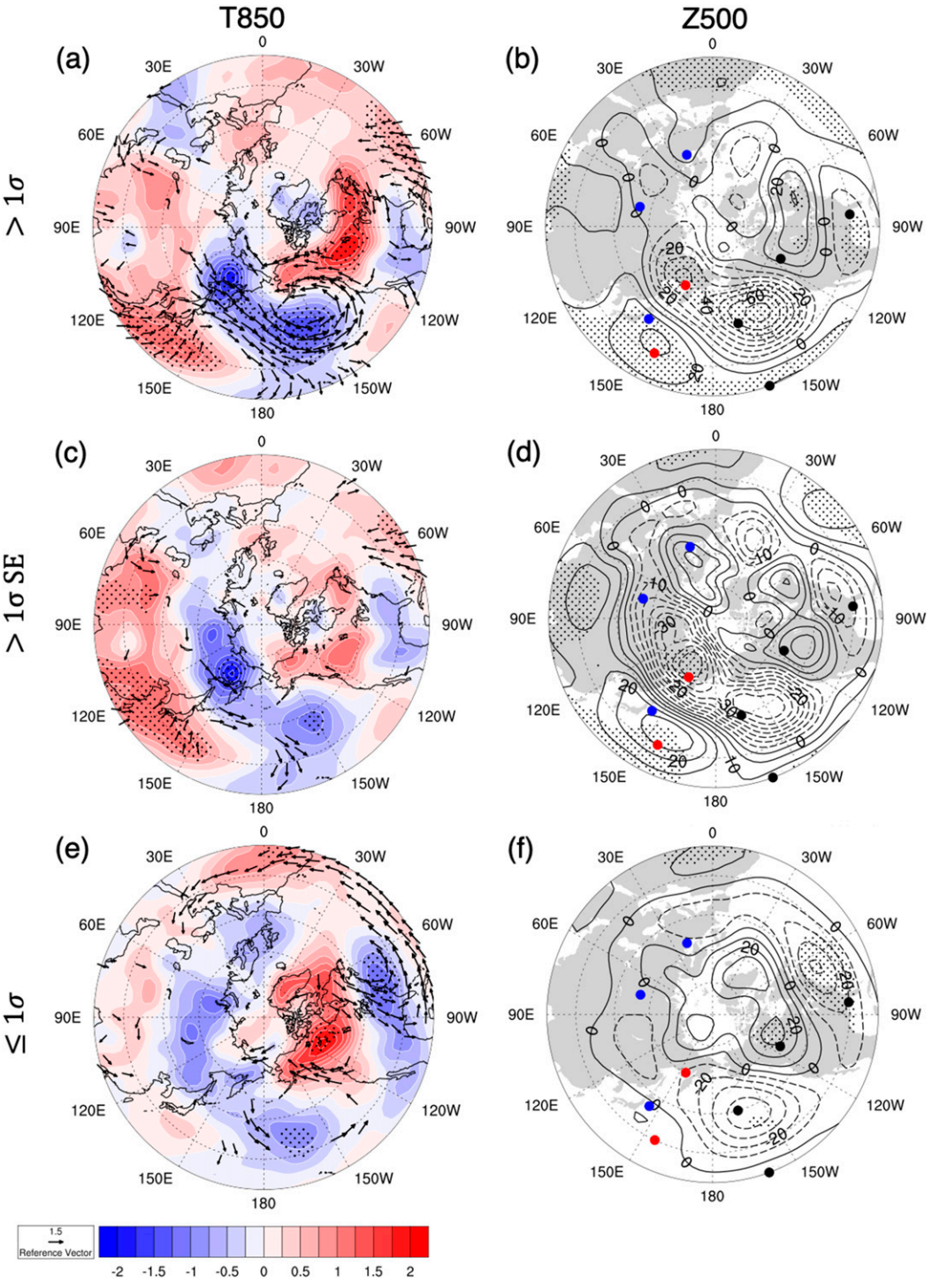

FIG. 12. As in Fig. 3, but for the (a),(b) $>1\sigma$ composites, (c),(d) $>1\sigma$ composites but with the super El Niño cases omitted, and (e),(f) $\leq 1\sigma$ composites based on the SST anomaly gradient near the date line.

positive SLP anomalies in the western Pacific Ocean are consistent with the warm winter in East Asia (Wang et al. 2000). In the eastern Pacific Ocean, the positive SST anomalies expanded to the date line in the developing spring and summer (Fig. 11a). This development modulated the activity of the Walker circulation and the modulation produces the IOD and subsequent basin warming in the Indian Ocean. Furthermore, the SST anomaly distribution in the Indian Ocean enhanced

TABLE 3. Teleconnection pattern indices for each reclassification.

	$>1\sigma$	$>1\sigma$ (without the super El Niño cases)	$\leq 1\sigma$
PNA	0.72	0.38	0.60
WP	−1.09	−0.98	−0.27
EU	−0.32	−0.38	−0.03

the suppression of convection in the western Pacific Ocean (Fig. 9b; Watanabe and Jin 2002).

This suppression is consistent with the divergent wind anomalies from the storm track in East Asia toward the western Pacific Ocean, corresponding to the weakened local Hadley circulation. This divergence acts as the negative Rossby wave source to create the anticyclonic circulation anomaly, the southern part of the WP pattern. Conversely, the lower-tropospheric positive heating anomaly in the Sea of Okhotsk contributes to reinforce the northern part of the WP pattern. Corresponding to this positive heating anomaly, the wave activity flux propagates northward from the positive Rossby wave source anomaly produced in the upper troposphere. This distribution of the positive heating anomaly evokes the increased sea ice extent in the Sea of Okhotsk, which in turn can induce a wave train, such as a cyclone anomaly over the eastern Sea of Okhotsk (approximately 60°N, 160°E), an anticyclone anomaly over the eastern Bering Sea (approximately 65°N, 145°W), and a cyclone anomaly over North America (approximately 50°N, 110°W; Honda et al. 1999). Therefore, the obscure PNA pattern in the warm winter composite can be interpreted as a result of overlapping with the wave train from the Sea of Okhotsk and the wave train related to the PNA pattern.

On the other hand, the non-warm winter composite was characterized by the dominant PNA pattern (Fig. 3f), the weak negative SST anomalies in the western Pacific Ocean, and a lack of the significant Indian Ocean basin warming. The positive SST anomalies in the eastern Pacific Ocean were located more to the east than that in the warm winter composite (Fig. 4c). This positive SST anomalies extend only to regions east of 120°W by the end of the developing summer and expanded to the date line in the developing fall (Fig. 11b). These SST distributions are consistent with slightly suppressed convection in the western Pacific Ocean and enhanced convection in the eastern Pacific Ocean (Fig. 9c). This enhanced convection in the equatorial central and eastern Pacific Ocean is consistent with the divergent wind anomalies that converged in the northern and in the northeastern Pacific Ocean. These convergences at the midlatitudes correspond to the second and fourth centers of action of the PNA pattern, respectively.

The discrepancies in the SST anomaly distribution between the warm and the non-warm winter composites are remarkable near the date line (Fig. 11c), persisting from the developing summer to the decaying spring. The gradient of the SST anomaly near the date line is large (small) in the warm (non-warm) winter composite consistent with the degree of the modulation of the Walker circulation.

To examine whether the gradient of the equatorial SST anomaly near the date line can be regarded as a precursory signal of the winter climate in the Far East, El Niño cases were reclassified by the gradient of the SST anomaly in JJA. The

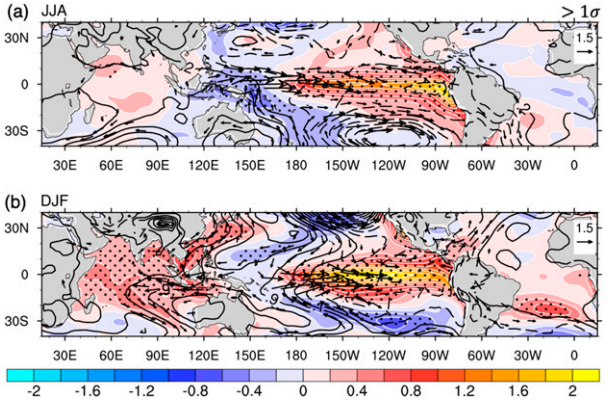

FIG. 13. SST (color shades; K), SLP (contours; hPa), and wind (arrows; m s^{-1}) anomalies at the 850-hPa surface in the DJF composite for (a) JJA and (b) DJF in $>1\sigma$ composite based on the SST anomaly gradient near the date line.

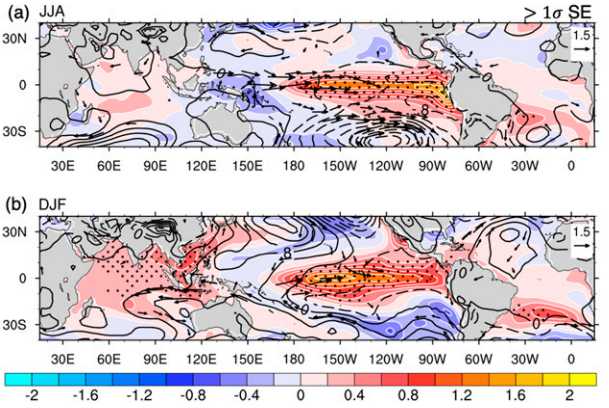

FIG. 14. As in Fig. 13, but without the super El Niño cases.

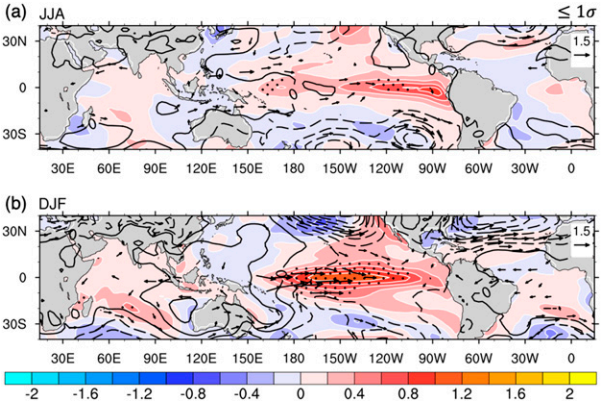

FIG. 15. As in Fig. 13, but for the $\leq 1\sigma$ composite based on the SST anomaly gradient near the date line.

reclassified composites of the height at the 500-hPa surface (Figs. 12a,b,e,f) and the SST and wind anomalies at the 850-hPa surface (Figs. 13 and 15) are analogous to the those in the warm and the non-warm winter composites (Figs. 3c–f and 4b,c). Similar features were found in the composite that omitted the three super El Niño cases (Figs. 12c,d and 14). Both composites based on the temperature at the 850-hPa surface in the Far East and on the gradient of the equatorial SST anomaly near the date line share the suppression in the western Pacific Ocean. Therefore, the suppressed convection in the western Pacific Ocean associated with the modulated Walker circulation plays an important role to influence on the winter climate in the Far East through the excitation of the WP pattern.

Two super El Niño cases were classified into the non-warm winter case and $\leq 1\sigma$ case. Distributions of SLP anomalies in East Asia are different between moderate EP, CP, and super El Niño (Garfinkel et al. 2019; Frauen et al. 2014). Those differences may explain the fact that two super El Niño cases show non-warm winter in the Far East. Furthermore, in this study, we found damping and reinforcement mechanisms for the PNA and WP patterns due to the modulated local Hadley circulation. Some proposed mechanisms for the excitation and maintenance of the PNA pattern exist, such as Rossby wave propagation for the tropical heat source (Horel and Wallace 1981; Hoskins and Karoly 1981) and formation by transient eddy vorticity flux in the North Pacific Ocean (Feldstein 2002; Franzke et al. 2011). On the other hand, the excitation and maintenance of the WP pattern were studied from the viewpoint of the planetary wave breaking in the upper troposphere (Takaya and Nakamura 2005a,b; Rivière 2010) and the available potential energy conversion from the climatological wind (Tanaka et al. 2016). However, these existing theories do not fully explain the mechanisms of the teleconnection patterns during El Niño and remain to be solved. To tackle these problems, numerical experiments and statistical analyses using daily or monthly datasets in the future studies may provide better insights into the mechanisms responsible for the teleconnection patterns produced during El Niño.

Acknowledgments. This study was supported by JSPS KAKENHI Grant 19H05698.

Data availability statement. The NOAA_ERSST_V5 data and NCEP Reanalysis data were provided by the NOAA/OAR/ESRL PSD, Boulder, Colorado, USA, from their website at https://www.esrl.noaa.gov/psd/. The JRA-55 datasets were provided by the JMA.

REFERENCES

Ashok, K., S. K. Behera, S. A. Rao, H. Weng, and T. Yamagata, 2007: El Niño Modoki and its possible teleconnection. *J. Geophys. Res.*, **112**, C11007, https://doi.org/10.1029/2006JC003798.

Feldstein, S. B., 2002: Fundamental mechanisms of the growth and decay of the PNA teleconnection pattern. *Quart. J. Roy. Meteor. Soc.*, **128**, 775–796, https://doi.org/10.1256/0035900021643683.

Feng, M., M. J. McPhaden, S.-P. Xie, and J. Hafner, 2013: La Niña forces unprecedented Leeuwin Current warming in 2011. *Sci. Rep.*, **3**, 1277, https://doi.org/10.1038/srep01277.

Franzke, C., S. B. Feldstein, and S. Lee, 2011: Synoptic analysis of the Pacific–North American teleconnection pattern. *Quart. J. Roy. Meteor. Soc.*, **137**, 329–346, https://doi.org/10.1002/qj.768.

Frauen, C., D. Dommenget, N. Tyrrell, M. Rezny, and S. Wales, 2014: Analysis of the nonlinearity of El Niño–Southern Oscillation teleconnections. *J. Climate*, **27**, 6225–6244, https://doi.org/10.1175/JCLI-D-13-00757.1.

Garfinkel, C. I., I. Weinberger, I. P. White, L. D. Oman, V. Aquila, and Y.-K. Lim, 2019: The salience of nonlinearities in the boreal winter response to ENSO: North Pacific and North America. *Climate Dyn.*, **52**, 4429–4446, https://doi.org/10.1007/s00382-018-4386-x.

Gill, A. E., 1980: Some simple solutions for heat-induced tropical circulation. *Quart. J. Roy. Meteor. Soc.*, **106**, 447–462, https://doi.org/10.1002/qj.49710644905.

Halpert, M. S., and C. F. Ropelewski, 1992: Surface temperature patterns associated with the Southern Oscillation. *J. Climate*, **5**, 577–593, https://doi.org/10.1175/1520-0442(1992)005<0577:STPAWT>2.0.CO;2.

Hameed, S. N., D. Jin, and V. Thilakan, 2018: A model for super El Niños. *Nat. Commun.*, **9**, 2528, https://doi.org/10.1038/s41467-018-04803-7.

Honda, M., K. Yamazaki, H. Nakamura, and K. Takeuchi, 1999: Dynamic and thermodynamic characteristics of atmospheric response to anomalous sea-ice extent in the Sea of Okhotsk. *J. Climate*, **12**, 3347–3358, https://doi.org/10.1175/1520-0442(1999)012<3347:DATCOA>2.0.CO;2.

Horel, J. D., and J. M. Wallace, 1981: Planetary-scale atmospheric phenomena associated with the Southern Oscillation. *Mon. Wea. Rev.*, **109**, 813–829, https://doi.org/10.1175/1520-0493(1981)109<0813:PSAPAW>2.0.CO;2.

Hoskins, B. J., and D. J. Karoly, 1981: The steady linear response of a spherical atmosphere to thermal and orographic forcing. *J. Atmos. Sci.*, **38**, 1179–1196, https://doi.org/10.1175/1520-0469(1981)038<1179:TSLROA>2.0.CO;2.

Huang, B., and Coauthors, 2017: Extended Reconstructed Sea Surface Temperature, version 5 (ERSSTv5): Upgrades, validations, and intercomparisons. *J. Climate*, **30**, 8179–8205, https://doi.org/10.1175/JCLI-D-16-0836.1.

Kalnay, E., and Coauthors, 1996: The NCEP/NCAR 40-Year Reanalysis Project. *Bull. Amer. Meteor. Soc.*, **77**, 437–472, https://doi.org/10.1175/1520-0477(1996)077<0437:TNYRP>2.0.CO;2.

Kao, H.-Y., and J.-Y. Yu, 2009: Contrasting eastern-Pacific and central-Pacific types of ENSO. *J. Climate*, **22**, 615–632, https://doi.org/10.1175/2008JCLI2309.1.

Kataoka, T., T. Tozuka, S. Behera, and T. Yamagata, 2014: On the Ningaloo Niño/Niña. *Climate Dyn.*, **43**, 1463–1482, https://doi.org/10.1007/s00382-013-1961-z.

Kobayashi, S., and Coauthors, 2015: The JRA-55 reanalysis: General specifications and basic characteristics. *J. Meteor. Soc. Japan*, **93**, 5–48, https://doi.org/10.2151/jmsj.2015-001.

Kodera, K., 1998: Consideration of the origin of the different midlatitude atmospheric responses among El Niño events. *J. Meteor. Soc. Japan*, **76**, 347–361, https://doi.org/10.2151/jmsj1965.76.3_347.

Matsuno, T., 1966: Quasi-geostrophic motions in the equatorial area. *J. Meteor. Soc. Japan*, **44**, 25–43, https://doi.org/10.2151/jmsj1965.44.1_25.

Ohba, M., and H. Ueda, 2005: Basin-wide warming in the equatorial Indian Ocean associated with El Niño. *SOLA*, **1**, 89–92, https://doi.org/10.1002/JOC.1482.

Rivière, G., 2010: Role of Rossby wave breaking in the west Pacific teleconnection. *Geophys. Res. Lett.*, **37**, L11802, https://doi.org/10.1029/2010GL043309.

Saji, N. H., B. N. Goswami, P. N. Vinayachandran, and T. Yamagata, 1999: A dipole mode in the tropical Indian Ocean. *Nature*, **401**, 360–363, https://doi.org/10.1038/43854.

Sardeshmukh, P. D., and B. J. Hoskins, 1988: The generation of global rotational flow by steady idealized tropical divergence. *J. Atmos. Sci.*, **45**, 1228–1251, https://doi.org/10.1175/1520-0469(1988)045<1228:TGOGRF>2.0.CO;2.

Shiozaki, M., and T. Enomoto, 2020: Comparison of the 2015/16 El Niño with the two previous strongest events. *SOLA*, **16**, 12–16, https://doi.org/10.2151/SOLA.2020-003.

Takaya, K., and H. Nakamura, 2001: A formulation of a phase-independent wave-activity flux for stationary and migratory quasigeostrophic eddies on a zonally varying basic flow. *J. Atmos. Sci.*, **58**, 608–627, https://doi.org/10.1175/1520-0469(2001)058<0608:AFOAPI>2.0.CO;2.

——, and ——, 2005a: Geographical dependence of upper-level blocking formation associated with intraseasonal amplification of the Siberian high. *J. Atmos. Sci.*, **62**, 4441–4449, https://doi.org/10.1175/JAS3628.1.

——, and ——, 2005b: Mechanisms of intraseasonal amplification of the cold Siberian high. *J. Atmos. Sci.*, **62**, 4423–4440, https://doi.org/10.1175/JAS3629.1.

——, and ——, 2013: Interannual variability of the East Asian winter monsoon and related modulations of the planetary waves. *J. Climate*, **26**, 9445–9461, https://doi.org/10.1175/JCLI-D-12-00842.1.

Tanaka, S., K. Nishii, and H. Nakamura, 2016: Vertical structure and energetics of the western Pacific teleconnection pattern. *J. Climate*, **29**, 6597–6616, https://doi.org/10.1175/JCLI-D-15-0549.1.

Ueda, H., A. Kibe, M. Saitoh, and T. Inoue, 2015: Snowfall variations in Japan and its linkage with tropical forcing. *Int. J. Climatol.*, **35**, 991–998, https://doi.org/10.1002/joc.4032.

Wallace, J. M., and D. S. Gutzler, 1981: Teleconnections in the geopotential height field during the Northern Hemisphere winter. *Mon. Wea. Rev.*, **109**, 784–812, https://doi.org/10.1175/1520-0493(1981)109<0784:TITGHF>2.0.CO;2.

Wang, B., R. Wu, and X. Fu, 2000: Pacific–East Asian teleconnection: How does ENSO affect East Asian climate? *J. Climate*, **13**, 1517–1536, https://doi.org/10.1175/1520-0442(2000)013<1517:PEATHD>2.0.CO;2.

Wang, L., and W. Chen, 2014: An intensity index for the East Asian winter monsoon. *J. Climate*, **27**, 2361–2374, https://doi.org/10.1175/JCLI-D-13-00086.1.

——, ——, and R. Huang, 2008: Interdecadal modulation of PDO on the impact of ENSO on the East Asian winter monsoon. *Geophys. Res. Lett.*, **35**, L20702, https://doi.org/10.1029/2008GL035287.

Watanabe, M., and F.-F. Jin, 2002: Role of Indian Ocean warming in the development of Philippine Sea anticyclone during ENSO. *Geophys. Res. Lett.*, **29**, 1478, https://doi.org/10.1029/2001GL014318.

Yuan, Y., and S. Yang, 2012: Impacts of different types of El Niño on the East Asian climate: Focus on ENSO cycles. *J. Climate*, **25**, 7702–7722, https://doi.org/10.1175/JCLI-D-11-00576.1.